5M.1

THE RESPONSE OF STATICALLY UNSTABLE OROGRAPHIC CLOUDS TO SMALL-SCALE TOPOGRAPHIC FEATURES

Daniel J. Kirshbaum*
George Bryan
Rich Rotunno
National Center for Atmospheric Research, Boulder, CO

and
Dale Durran
University of Washington, Seattle, WA

1 Introduction

Recent observations have shown that coastal mountain ranges tend to trigger quasi-stationary rainbands in potentially unstable cross-barrier flows. Miniscloux et al. (2001) found that rainbands formed parallel to the low-level flow during two convective rain events of the Cévennes experiment in southern France. These "static" bands, embedded within a time-evolving larger-scale precipitation field, produced precipitation enhancements of up to 100 mm day^{-1}. In the western Kyushu region of Japan, long-lived rainbands were observed by Yoshizaki et al. (2000) to dominate the precipitation signature in the lee of small hills. Remarkably coherent and stationary rainbands were also observed over the Coastal Range in western Oregon (Kirshbaum and Durran, 2005b). These bands produced cumulative rainfall of up to 69 mm on the ridge upslope over a six-hour period.

Different theories exist to explain the stationary rainbands in the three studies just mentioned. Cosma et al. (2002) suggested that the bands in Miniscloux et al. (2001) were triggered by lee-side convergence patterns caused by isolated topographic obstacles, while Yoshizaki et al. (2000) hypothesized that small-scale hills trigger convective cells that are subsequently organized into linear elements by vertical wind shear and preexisting mesoscale convergence zones in the larger-scale flow. Kirshbaum and Durran (2005a) suggested that both vertical shear and lee waves triggered by small-scale obstacles just upstream of the orographic cloud were able to organize convection into bands, though only the latter produced steady rainbands with substantial localized precipitation accumulations.

Although quasi-stationary orographic rainbands have potentially important atmospheric and hydrological implications, the dynamics behind the formation of the bands, as well as their preferred physical scales, is still under debate. In the following we investigate the triggering and organization of the rainbands through numerical simulation. The experiments suggest that bands may be triggered by either hills or valleys that lie just upstream of the orographic cap cloud, and that both the organization and stationarity of the bands is a result of their fixed triggering source.

2 Methodology

2.1 Numerical model

The numerical experiments are conducted with a mesoscale cloud-resolving model whose formulation and implementation is described in Bryan and Fritsch (2002). Rotational effects are neglected due to the high characteristic Rossby numbers of the mesoscale flows under consideration, micro-

**Corresponding author address:* Daniel Kirshbaum; NCAR/MMM; P.O. Box 3000; Boulder, CO 80302;email:kirshbau@ucar.edu

physical processes are represented by a Kessler warm rain parameterization, and subgrid-scale turbulence is parameterized using a first-order closure scheme (Lilly, 1962). A rayleigh upper boundary condition is applied over the highest four km of the model domain, radiation conditions are imposed at the $x-$ boundaries, and periodicity is imposed at the $y-$ boundaries.

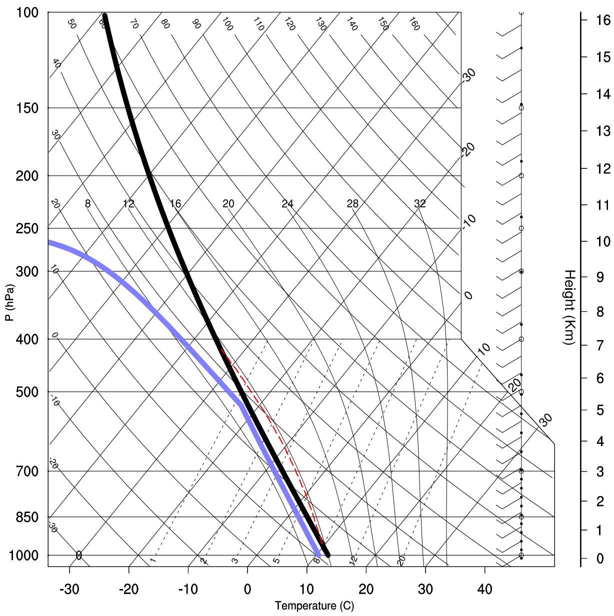

Figure 1: Skew-T profile of upstream sounding used for all the simulations. Temperature profile is shown in black, dewpoint is in blue, and the temperature of a lifted surface parcel in red.

2.2 Upstream flow

The upstream flow for all the simulations is based on the undisturbed conditions upstream of the Coastal Range estimated by Kirshbaum and Durran (2005b) during the 12-13 November 2002 post-frontal precipition event. A simplified approximation to that moist yet unsaturated thermodynamic profile is obtained by first setting the Brunt-Väisälä frequency N to $0.01\ \mathrm{s}^{-1}$ over the depth of the domain, which has a height of $L_z = 16$ km. The relative humidity is 90% over the lowest five kilometers, which decreases linearly to 1% at $z = 10$ km and remains constant at 1% to the top of the domain. These parameter specifications result in potential instability ($d\theta_e/dz < 0$) over the lowest 2.5 km. The wind profile is approximated by a uniform speed U of $10\ \mathrm{ms}^{-1}$ oriented at an angle $\Theta = 230°$ CCW from due north (note that Θ is set to $270°$ in the idealized simulations of section 4). Profiles of temperature, dewpoint, and wind vectors are displayed in Fig. 1, indicating conditional stability at low levels, absolute stability aloft, and a wind profile that is uniform with height.

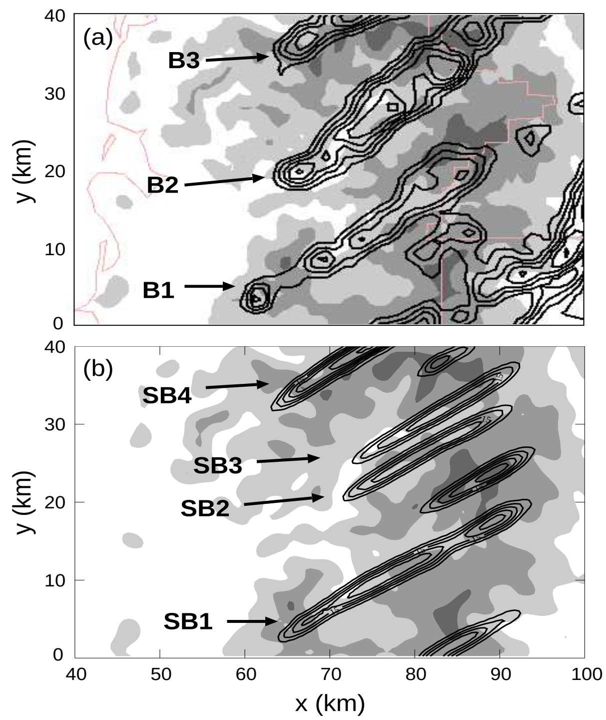

Figure 2: Comparison of observed (a) and simulated (b) radar reflectivities. Contour interval of reflectivity is 5 dBZ; contour interval of underlying topography is 250 m.

3 Simulations

3.1 12 November 2002 case

We first perform a simulation using the sounding just described and the real Coastal Range topography to determine if the model can adequately reproduce the observations from the 12-13 Nov. 2002 event. The topographic profile used for this simulation (REAL) is obtained from the database of global USGS data (“GTOPO30”) with a horizontal resolution of 120 pts/deg, which gives a meridional grid spacing of 930 m and a zonal grid spacing of 660 m at $45°$ N latitude. The numerical domain includes a quasi-2D section of the topography (see Fig. 4a) that is centered at a latitude of $45.5°$ N and $-123.5°$ E and is 40 km long in the $y-$direction and $L_x = 160$ km long in the $x-$direction. This raw data is linearly interpolated to a horizontal resolution $\Delta = \Delta x = \Delta y$ of 500 m then folded around the $y = 40$ km axis so that it is a mirror image of itself over $40 < y \leq 80$ km, which ensures periodicity at the $y-$boundaries and gives $L_y = 80$ km. Finally, to avoid excitation of poorly-resolved numerical modes, this periodic topography is Fourier-transformed to wavenumber space and all topographic power at wavenumbers greater than or equal to $\frac{2\pi}{6\Delta x}$ is removed.

A comparison of radar reflectivity between the observations and the REAL simulation in Fig. 2 illustrates the numerical model's accurate reproduction of the basic precipitation pattern observed in this case. Radar reflectivity at 2003 UTC on 12 Nov. 2002 (Fig. 2a) is smoothed by a nine-point spatial filter and overlaid on the topography, which is contoured in grayscale at 250-m intervals. The simulated reflectivity at $t = 4$ h and $z = 1.5$ km (Fig. 2b) is computed from model variables using the expression $Z = 2.4 \times 10^4 (\rho_{\rm dry} q_r)^{1.83}$ (Douglas, 1964) and smoothed by a 25-point filter, whose higher order is necessary to account for the higher horizontal resolution of the simulation (500 m) than the radar data (nominally 1 km). Note that (Fig. 2b) only shows the response over $0 \leq y \leq 40$ km, the unfolded half of the domain where the simulated topography corresponds to reality. Both the observed and simulated reflectivity exhibit a highly organized appearance with several well-defined bands, some of which are clearly collocated like bands B1 and B3 (Fig. 2a) with bands SB1 and SB4 (Fig. 2b). The only obvious difference is that the observed band SB2 is composed of two separate bands in the simulation, reflecting a slightly smaller scale convective pattern.

3.2 Towards a more idealized framework

A few steps are taken to smoothly transition from the REAL simulation described above to a more idealized framework suited for systematic investigation of orographic rainbands. First we reduce the size of the computational domain by considering only the $20 \leq y \leq 60$ km portion of the Coastal Range topography in Fig. 2, which reduces L_y from 80 km to 40 km and lessens the computational expense. Next we rotate Θ from $235°$ to $270°$ so that the wind is directed purely across the 1D barrier. A simulation identical to the REAL case except for these two changes (REAL-SM) generates a banded cloud liquid water (q_c) field in Fig. 3b whose band orientations have rotated in phase with the wind shift and are slightly more numerous per unit length (9 bands over $L_y = 40$ km) than the bands in the the REAL simulation (12 bands over $L_y = 80$ in Fig. 3a). This increase in band concentration in the REAL-SM simulation is associated with the effectively larger projection of the wind upon the mesoscale mountain ridge, which is given by the cosine of Θ.

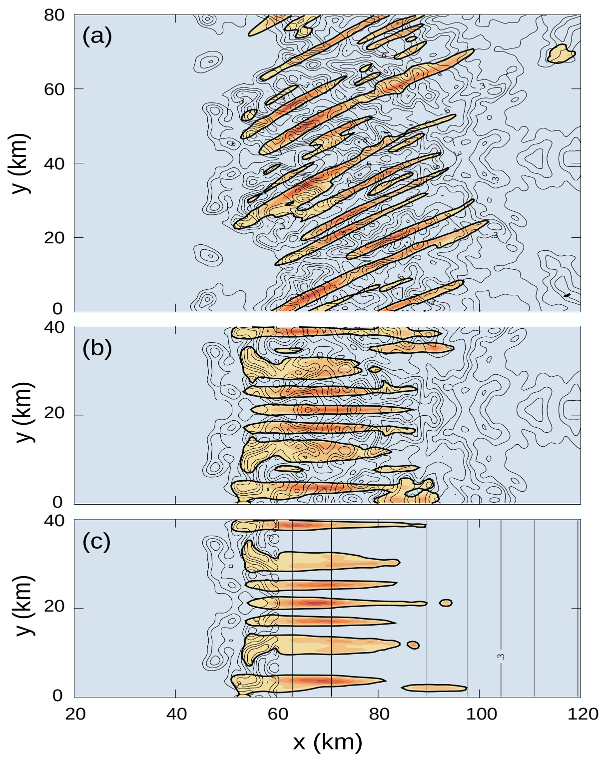

Figure 3: Cloud liquid water fields at $t = 4$ h and $z = 1.5$ km for the (a) REAL, (b) REAL-SM, and (c) REAL-PATCH simulations. Contours of q_c are 2×10^{-4} kg/kg. Topographic contours are 100 m.

The mountainous topography $h(x, y)$ from the REAL and REAL-SM simulations is made up of two basic scales with very different dynamical effects. The first is a 1D mesoscale ridge $h_m(x)$ responsible for gradually lifting the impinging flow to saturation and destabilizing it, and the second is small-scale 2D perturbations on the mountain $h_s(x, y)$ that trigger convective growth. These two components may be separated by taking the Fourier transform $H(k, l)$ of the topography $h(x, y)$ and partitioning H into a mesoscale component $H_{\rm m}(k)$ containing all Fourier coefficients satisfying $\kappa = \left(k^2 + l^2\right)^{1/2} \leq \kappa_{\rm m} = \frac{2\pi}{L_{\rm m}}$, where $L_m = 50$ km,

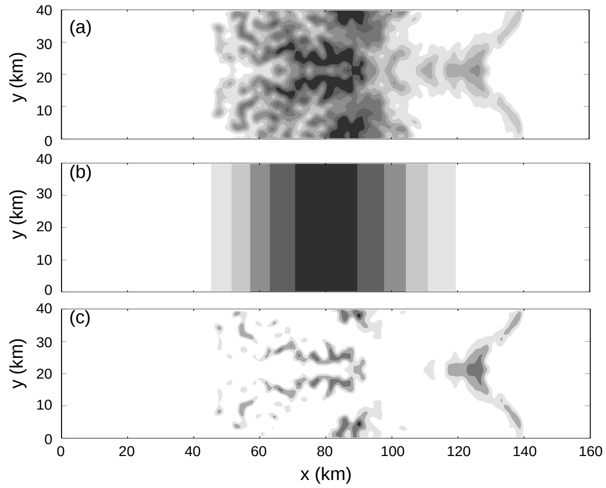

Figure 4: Decomposition of real terrain h (a) into mesoscale h_m (b) and small-scale h_s (c) components. Contour interval is 100 m.

and a small-scale component $H_s(k, l)$ consisting of the remaining high-wavenumber coefficients ($\kappa > \kappa_m$). This decomposition is performed on the REAL-SM terrain in Fig. 4. The entire topography h is redisplayed in Fig. 4a, which contains a 1D mesoscale component (h_m in Fig. 4b), and a 2D small-scale component (h_s in Fig. 4c) that is a random-looking collection of low-amplitude bumps located primarily in the center of the domain.

To determine the importance of the small-scale topography just upstream of the bands on the convective response, we perform a simulation (REAL-PATCH) that makes use of the topographic decomposition just described by specifying the terrain to be a piecewise function of h_s and h_m

$$h(x,y) = \begin{cases} h_m(x) & : \quad x < 40\text{km} \\ h_m(x) + h_{\text{ss}}(x,y) & : \quad 40 \le x \le 60\text{km} \\ h_m(x) & : \quad x > 60\text{km}, \end{cases} \tag{1}$$

resulting in a topography that is irregular over a small patch upstream of the mountain ridge and a smoothly-varying hill everywhere else. This topography is overlaid by the q_c field at $t = 4$ h and $z = 1.5$ km in Fig. 3c, indicating that the convective response is nearly identical to the REAL-SM case (Fig. 3b). This remarkable agreement in the q_c fields of these cases suggests that the behavior of orographic rainbands is predominantly controlled by the small-scale topography well upstream of the ridge crest, not by features closer to the mountain summit.

3.3 Dynamics behind the triggering

The dynamical processes behind orographic rainbands are investigated by a series of three simulations that use the same mesoscale topography h_m as in the previous simulations but an h_s that is made up of a column of small-scale sinusoidal bumps at a fixed $x-$location (x_0)

$$h_s = \begin{cases} 0 & : \quad x_b < -\frac{\lambda_b}{4} \\ H_b \sin\left(\frac{2\pi x_b}{\lambda_b}\right) \cos\left(\frac{2\pi y}{\lambda_b}\right) & : \quad -\frac{\lambda_b}{4} \le x_b \le \frac{\lambda_b}{4} \\ 0 & : \quad x_b > \frac{\lambda_b}{4}, \end{cases} \tag{2}$$

where $x_b = x - x_0$, $\lambda_b = 10$ km is the wavelength and $H_b = 100$ m the amplitude of the bumps. In the first simulation (IDEAL-B10-x40) we choose $x_0 = 40$ km, the upstream end of the 20-km-long noise patch that was just shown to dominate the convective behavior in the REAL-SM simulation. This topography is overlaid by the q_c field of this simulation at $z = 1.5$ km and $t = 4$ h in Fig. 5, showing that a well-organized band forms downstream of each bump in the small-scale terrain at $x = 40$ km.

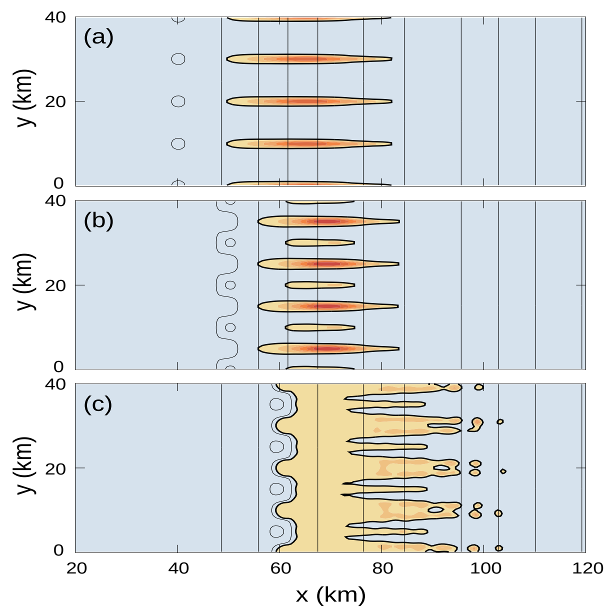

Figure 5: As in Fig. 3, except for the (a) IDEAL-B10-x40, (b) IDEAL-B10-x50, and (c) IDEAL-B10-x60 simulations. Contour interval is 2×10^{-4} kg/kg; topographic contours are 100 m.

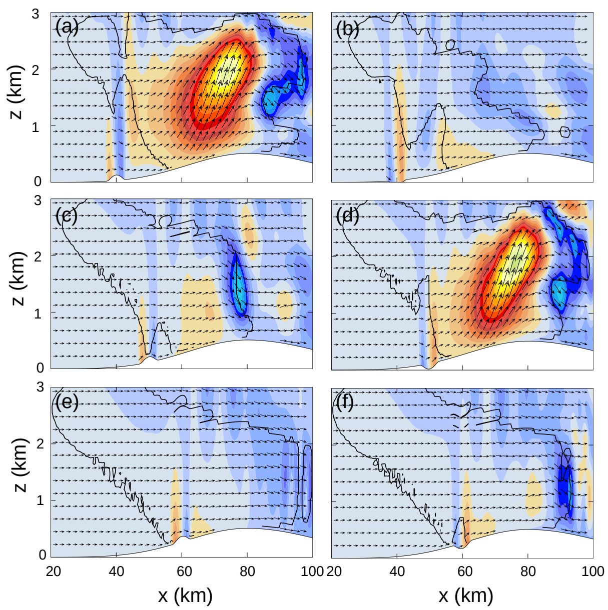

Figure 6: Vertical cross sections of w, cloud outline ($q_c = 1 \times 10^{-6}$), and plane-parallel velocity vectors at $t = 4$ h for (a)-(b) the IDEAL-B10-x40 simulation at $y = 20$ and $y = 25$ km, (c)-(d) the IDEAL-B10-x50 simulation at $y = 20$ and $y = 25$ km, and (e)-(f) the IDEAL-B10-x60 simulation at $y = 20$ and $y = 25$ km. Contour interval for w is 0.15 m/s, with positive values in reddish colors and negative values in blue.

The vertical structures of w, q_c, and plane-parallel velocity vectors both inside and between the bands in the IDEAL-B10-x40 simulation are compared in Fig. 6a-b, showing that the upstream edge of the cloud at $y = 20$ km (Fig. 6a) is co-incident with an elevated positive vertical velocity (w) perturbation past the bump at $x = 40$ km. Similar $w-$perturbations are found at the leading edges of all the convective bands in this simulation (Fig. 5b), suggesting that each bump induces an elevated updraft that brings the conditionally unstable low-level flow to saturation and its level of free convection (LFC). As discussed by Kirshbaum and Durran (2005a), these elevated updrafts are nonhydrostatic lee waves generated by stable flow over small-scale topography just upstream of the main orographic cap cloud, which increase the vertical motion at the cloud's leading edge.

Halfway between two bands at $y = 25$ km (Fig. 6b), h_s becomes negative and the lee-wave perturbations are reversed in sign from Fig. 6a. A downdraft now exists in the same location ($x \sim 50$ km) where an updraft triggered convection at $y = 20$ km (Fig. 6a). Despite the partial saturation caused by the lee wave updraft at $x \sim 42$ km, the flow encounters another region of descent at $x \sim 50$ km that rapidly dries the lowest layers. By this time the flow past the bumps (Fig. 6a) has already started amplifying convectively and the compensating subsidence from these updrafts suppresses the convection in the saturated flow further downstream of the dips ($x > 60$ km).

A second simulation (IDEAL-B10-x50) is performed where x_0 is shifted 10 km downstream, resulting in a pattern of convective bands (Fig. 5b) similar to the IDEAL-B10-x40 case (Fig. 5a) except that the strongest four bands are now positioned downstream of the valleys rather than the hills. The vertical cross-section at $y = 20$ km in Fig. 6c shows a potential flow pattern over the hill in which saturation is reached on its upslope and then immediately followed by rapid descent and partial desaturation. This contrasts with the flow at $y = 25$ km (Fig. 6c), which dries as it descends into the valley and saturates on its lee side, triggering a strong convective band. As in the IDEAL-B10-x40 simulation, convection in this case is triggered by the lee-wave updraft that lies closest to the main orographic cap cloud and is not followed by any lee-wave downdrafts.

A fundamentally different convective response is obtained when x_0 is shifted 10 km further downstream in the final simulation (IDEAL-B10-x60 in Fig. 5c). Convection past the bumpy terrain is weak and no well-defined bands are apparent. The vertical cross-sections of w and q_c in Fig. 6e-f indicate that the bumps and the valleys are now both located inside the main orographic cloud where the flow is statically unstable. Unlike the previous cases where lee waves within a mostly dry environment triggered moist convection, the small-scale terrain in this case induces a potential flow pattern in the cloud where parcels are essentially returned to their original level of buoyancy and do not ascend rapidly after the perturbation.

4 Bandedness: a (preliminary) conceptual model

The strongly banded responses in the IDEAL-B10-x40 and IDEAL-B10-x50 simulations may be explained through a conceptual model based on the IDEAL-B10-x40 case in Fig. 7. As shown in Fig. 6, convection is first triggered when lee-wave updrafts over small-scale topographic obstacles just upstream of the main orographic cloud bring the flow to its LFC. In the absence of sufficient subsequent descent to desaturate the cloud, convective perturbations amplify as they advect downstream. Rather than aligning upright like cellular convection, however, the convective updrafts tilt downstream (c.f. Fig.6) because their upstream edges are fixed to the stationary triggering source. The downstream tilt α of the plumes depends on the ratio of the ground-relative velocities ($\alpha = \tan^{-1}(u/w)$), which is equal to the direction of the plane-parallel flow in an $x - z$ cross-section. In the IDEAL-B10-x40 and IDEAL-B10-x50 cases the updrafts are nearly horizontal ($\alpha =\sim 80°$), which creates a banded cloud pattern with compensating downdrafts that suppress convection in-between.

5 Conclusions

Quasi-stationary orographic rainbands are a common phenomenon over coastal mountain ranges that can greatly increase the spatial variability of precipitation. These bands may be triggered in moist, potentially unstable flows by small-scale topographic obstacles embedded upon a larger-scale ridge, such as in the post-frontal precipitation event over the Oregon Coastal Range on 12-13 September 2002. This study has used data from that event as a guideline for the numerical investigation of orographic rainbands. The upstream flow was an approximation to the upstream flow during that event, which was characterized by high moisture and slight potential instability at low levels. The simulations performed showed a number of interesting features of these bands, including (1) the band dynamics are predominantly governed by the small-scale topography just upstream of the orographic cap cloud, (2) triggering is caused by lee-wave circulations induced by the small-scale topography, (3) either bumps or valleys may trigger convection depending on the location of their lee waves relative to the cap cloud, and (4) topographic perturbations inside the cap cloud have very little effect on the convection.

A primilinary conceptual model (Fig. 7) was presented to explain the location, steadiness, and bandedness of the orographic convection. In the model, band formation involved three basic processes: convection is first triggered by the lee-wave updraft closest to the cap cloud, next the convective updraft fixed to the lee-wave updraft becomes strongly tilted is it amplifies downstream, and finally the compensating subsidence caused by these updrafts suppresses convection in-between the bands, leading to a highly organized cloud pattern. Ongoing work in this area involves testing and refining the hypothesis presented above and learning the atmospheric and terrain-related parameters that control the stationary and organization of the bands. Another closely related project that is underway is to determine the preferred physical scales of the rainbands as a function of the input topography.

References

Bryan, G. H. and J. M. Fritsch, 2002: Moist absolute instability: The sixth static stability state. *Mon. Wea. Rev.*, **130**, 2917–2928.

Cosma, S., E. Richard, and F. Miniscloux, 2002: The role of small-scale orographic features in the spatial distribution of precipitation. *Quart. J. Roy. Meteor. Soc.*, **128**, 75–92.

Douglas, R. H., 1964: Hail size distributions. In *Proc. Conf. on Radio Meteor. and the 11th Wea. Rad. Conf.*, Boulder, Colorado, 146-149.

Kirshbaum, D. J. and D. R. Durran, 2005a: Atmospheric factors governing banded orographic convection. *J. Atmos. Sci.*, **62**. in press.

Kirshbaum, D. J. and D. R. Durran, 2005b: Observations and modeling of banded orographic convection. *J. Atmos. Sci.*, **62**, 1463–1479.

Lilly, D. K., 1962: On the numerical simulation of buoyant convection. *Tellus*, **14**, 148–172.

Miniscloux, F., J. D. Creutin, and S. Anquetin, 2001: Geostatistical analysis of orographic rainbands. *J. Appl. Meteorol.*, **40**, 1835–1854.

Yoshizaki, M., T. Kato, Y. Tanaka, H. Takayama, Y. Shoji, and H. Seko, 2000: Analytical and numerical study of the 26 june 1998 orographic rainband observed in western kyushu, japan. *J. Meteor. Soc. Japan*, **78**, 835–856.

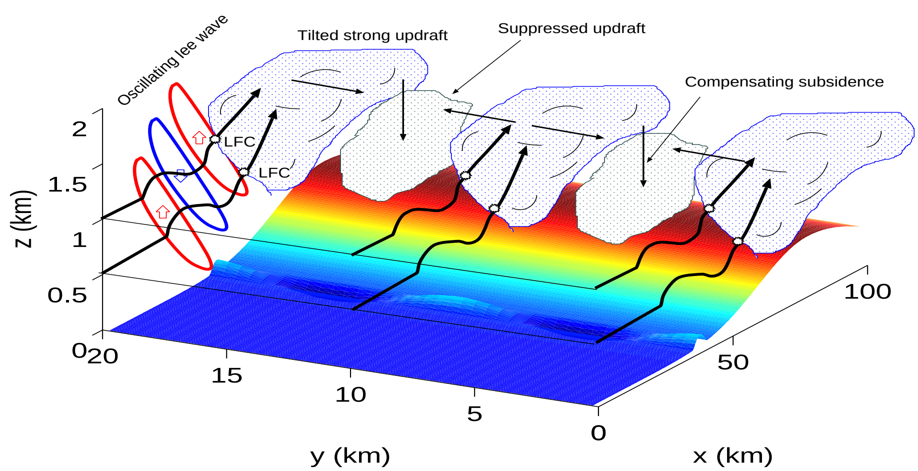

Figure 7: Conceptual model of band formation. Lee-wave perturbations are colored red to indicate updrafts and blue for downdrafts (as shown by the arrows inside). Streamlines of the low-level flow, as well as the buoyancy-driven return circulations, are shown by heavy black lines. Asterisks at the leading cloud edge are located where the LFC is reached by the ascending parcels.